Double Bubbles Sans Toil and Trouble:
Discrete Circulation-Preserving Vortex Sheets for Soap Films and Foams

Fang Da
Columbia University

Christopher Batty
University of Waterloo

Chris Wojtan
IST Austria

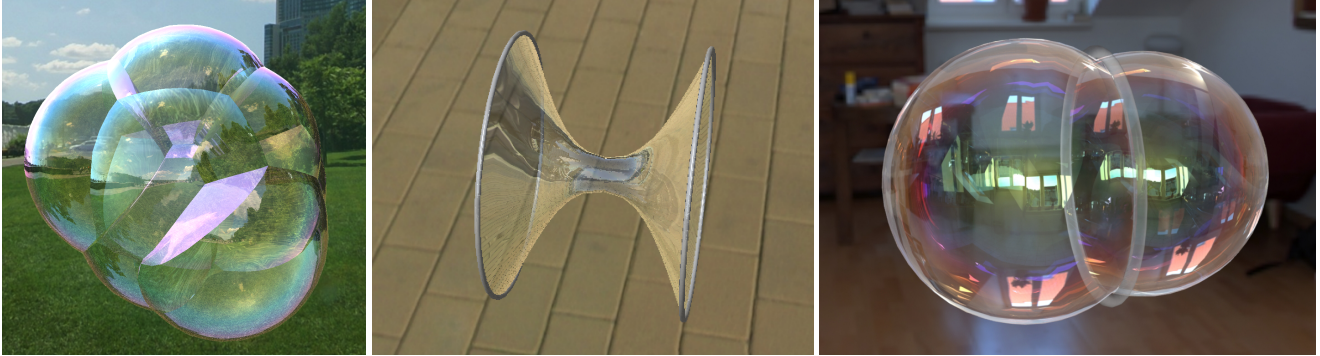Eitan Grinspun
Columbia University

Figure 1: *A variety of dynamic foam, film, and bubble scenarios captured by our method. Left: A small foam rearranges and settles to equilibrium. Center: A snapshot of an evolving catenoid soap film joining two circular wires, an instant before the film pinches apart. Right: A bubble with a wire constricting its mid-section gradually squeezes to one side.*

Abstract

Simulating the delightful dynamics of soap films, bubbles, and foams has traditionally required the use of a fully three-dimensional many-phase Navier-Stokes solver, even though their visual appearance is completely dominated by the thin liquid surface. We depart from earlier work on soap bubbles and foams by noting that their dynamics are naturally described by a Lagrangian vortex sheet model in which *circulation* is the primary variable. This leads us to derive a novel circulation-preserving surface-only discretization of foam dynamics driven by surface tension on a non-manifold triangle mesh. We represent the surface using a mesh-based multimaterial surface tracker which supports complex bubble topology changes, and evolve the surface according to the ambient air flow induced by a scalar circulation field stored on the mesh. Surface tension forces give rise to a simple update rule for circulation, even at non-manifold Plateau borders, based on a discrete measure of signed scalar mean curvature. We further incorporate vertex constraints to enable the interaction of soap films with wires. The result is a method that is at once simple, robust, and efficient, yet able to capture an array of soap films behaviors including foam rearrangement, catenoid collapse, blowing bubbles, and double bubbles being pulled apart.

CR Categories: I.6.8 [Simulation and Modeling]: Types of Simulation—Animation

Keywords: fluids, vortex sheet, circulation, non-manifold mesh

1 Introduction

Although we encounter bubbles and foam on a daily basis while drinking coffee, washing the dishes, or playing with children's toys, the motion and structure of these phenomena are difficult to understand and even more difficult to simulate with a computer.

Soap bubbles are essentially layers of immiscible fluids: air on the inside, a thin film of liquid, and then air on the outside again. The surface tension of the liquid drives the bubble toward a shape with less surface area, while air pressure forces the bubble to maintain a constant volume. These behaviors are described by the Navier-Stokes equations, which can be exceptionally difficult to solve accurately, especially when confronted with the large density jumps, immiscible fluid interfaces, stiff surface tension forces, and extremely thin liquid surfaces required for bubble motion.

Prior work has successfully simulated foam dynamics using an Eulerian approach. These approaches utilize considerable computational resources for the detailed calculation of the air dynamics within each bubble and the accurate resolution of film geometry. We propose a new model which solves the problem more economically while guaranteeing several important theoretical properties by construction.

Our proposed model is the first numerical method for the dynamics of soap films, bubbles, and foams that is based on the equations of non-manifold vortex sheets.

We model soap film structures as non-manifold vortex sheets driven by surface tension forces. We propose a discrete model to evolve the sheet as it deforms and undergoes topology changes such as pinching, merging, and rearrangement.

We represent the geometry using a Lagrangian non-manifold triangle mesh decorated with material region tags. We store *circulation* variables on the vertices; by Kelvin's circulation theorem this ensures a circulation-preserving model *by construction*. Numerical results exhibit nearly dissipation-free dynamics.

The use of the vortex sheet equations ensures an exactly divergence-free velocity field via the Biot-Savart law, and integrating mesh

vertex positions through the induced velocity field leads to excellent volume preservation over long simulations.

We derive a simple, discrete update rule for the effect of surface tension forces on the non-manifold sheet, based on a discrete measure of mean curvature. We formulate the update rule in a manner that generalizes immediately to the case of non-manifold junctions. This yields stable film behavior even along complex foam junctions. Through the addition of a simple vertex constraint mechanism, we support wire loops and structures to control the bubbles and films, enabling a variety of familiar bubble interactions.

Our complete computational model provides a compact description of foam dynamics that requires no volumetric discretization or linear system solve, is computationally efficient as compared to traditional Eulerian techniques, and is robust enough to animate complicated foam dynamics on a standard workstation.

2 Related Work

The behaviors of bubbles and foams are a subject of substantial interest across a variety of scientific and engineering disciplines (e.g., [Weaire and Hutzler 2001; Weaire 2013; Saye and Sethian 2013]). The reproduction of their visual characteristics was addressed in a pair of articles by Glassner [2000a; 2000b]; more recent authors have explored the dynamic simulation of bubbles.

Particulate Bubbles   One simple approach to small-scale bubble dynamics is to treat each bubble as a particle, with various rules controlling their interactions, such as the early work of Kück et al. [2002]. Later work has yielded increasingly realistic behavior, and often used these models to add bubble details to traditional volumetric liquid simulations [Greenwood and House 2004; Hong et al. 2008; Kim et al. 2010; Busaryev et al. 2012; Patkar et al. 2013].

Eulerian Bubbles   A different albeit more expensive tack is to model the bubbles themselves with volumetric *multiphase* fluid simulations. Since the thickness of the bubble's liquid film is on the order of micrometers, its mass is effectively negligible and can be treated as such; thus the main challenges are to simulate the air flow interior to the bubble with appropriate surface tension forces on the interface, and to represent the evolving non-manifold geometric structure of foams. Hong and Kim [2003] were the first in graphics to make use of a multiphase flow solver to model bubbles, applying surface tension as a smoothed body force. Hong and Kim [2005] adapted earlier work in computational physics [Kang et al. 2000], using ghost-fluid methods to incorporate surface tension boundary conditions for fully submerged bubbles. In a similar vein, Mihalef et al. [2006] simulated boiling water. To allow multiple bubbles in mutual contact and thereby support foam structures, Zheng et al. [2006] presented a regional level set method that generalizes the standard level set method to more than two regions. Zheng et al. also proposed a semi-implicit surface tension discretization to improve stability. Losasso et al. [2006] similarly extended the particle level set method to many regions to adapt Hong's work to the case of multiple interacting liquids. Kim et al. [2007] artificially inflated bubbles to compensate for volume drift. Saye and Sethian [2013] added a model for film drainage operating on different time scales.

Mesh-Based Bubbles   Since the visual appearance of bubbles is entirely dominated by the soap film itself, a seemingly natural approach is to focus modeling efforts there. Ďurikovič [2001] proposed such a method in which the bubble surface is represented by a deformable mass-spring system on a triangle mesh. Simple surface tension forces based on the Laplace-Young equation are applied to the vertices, assuming bubbles maintain a near-spherical configuration. Similarly, Brochu [2006] proposed a preliminary boundary-element discretization of 2D droplet dynamics, and Zhang et al. [2012] used a surface-only mass-spring model for real-time animation of triangulated liquid droplets. Batty et al. [2012] modeled thin sheets of viscous liquid with surface tension using triangle meshes, but did not address bubbles. Though computationally attractive, these models concentrate the mass of the system on the (thin) liquid film, whereas in the case of bubbles the film is effectively massless relative to the surrounding air flow. Zhu et al. [2014] applied a similar thin-sheet idea to inviscid liquids and films, and modeled the influence of wind by coupling to a standard dense Eulerian grid method. This approach yielded compelling animations of blowing bubbles, soap film catenoids pinching apart, and waterbell shapes, though it cannot model multi-bubble foam structures.

A more accurate approach to mesh-based modeling of bubbles and foams *at equilibrium* is to construct a discrete surface energy based on the area of the interfaces subject to a volume constraint per bubble, and seek to minimize it. This is the approach taken by the venerable *Surface Evolver* technique [Brakke 1992]. Since surface tension forces are proportional to interface mean curvature, the resulting discrete surface energy gradient in this model is essentially equivalent to discrete mean curvature operators common in graphics [Pinkall and Polthier 1993; Meyer et al. 2002]. Recent work on constant-mean-curvature surfaces [Pan et al. 2012] modifies the energy functional to simultaneously optimize mesh quality.

Methods for volumetric simulation of multiphase flows have also made use of explicit moving meshes. For example, conforming Lagrangian tetrahedral meshes with dynamic remeshing allow for a finite element discretization of multiple regions with area-based surface tension discretized on the interface triangles [Misztal et al. 2012; Clausen et al. 2013]. Rather than use a volumetric tetrahedral mesh, Da et al. [2014] presented *Los Topos*, a multi-region extension of the *El Topo* triangulated mesh-based surface tracking package [Brochu and Bridson 2009], and applied it to Eulerian grid-based volumetric multiphase liquids. Our work makes use of *Los Topos* to handle the complex topological rearrangements exhibited by foams. In general, these mesh-based volumetric methods rely on a complete discretization of the fluid domain, rather than the surface alone, and have not been applied to bubble dynamics.

Vortex-Based Fluids   Vortex methods model incompressible flows by relying on an alternative basis representation [Cottet and Koumoutsakos 2000]. Rather than choosing the primary variable to be velocity, which must be constrained to lie in the space of incompressible vector fields, vortex methods evolve the dynamics using the curl of velocity, or *vorticity*, $\omega = \nabla \times \mathbf{u}$. This family of methods guarantees incompressibility by construction, avoids numerical dissipation common to traditional methods, and provides a terser representation of the velocity field.

A variety of Lagrangian discretizations of the vorticity equation have been used including particles [Park and Kim 2005], filaments [Angelidis and Neyret 2005; Angelidis et al. 2006; Weissmann and Pinkall 2009; Weissmann and Pinkall 2010; Barnat and Pollard 2012], and sheets [Pfaff et al. 2012; Brochu et al. 2012], along with circulation-based Eulerian discretizations [Elcott et al. 2007]. The conserved variable in all of these cases is circulation, though Mullen et al. [2009] presented an interesting *energy-preserving* Eulerian discretization. Zhang and Bridson [2014] recently proposed an improved Particle-Particle Particle-Mesh (PPPM) strategy to accelerate the major bottleneck in Lagrangian vorticity-based schemes: evaluation of the Biot-Savart kernel to reconstruct the velocity field. Earlier work used the Fast Multipole Method (FMM) [Brochu et al. 2012], truncated the required kernel evaluations [Pfaff et al. 2012; Vines

et al. 2014], or suffered the $O(N^2)$ cost of pairwise evaluation.

Although vortex methods are most commonly applied to smoke, a few authors have considered the role of vortex sheets at or near a liquid interface. Golas et al. [2012] used a hybrid approach: a vortex particle method handles the large interior of the flow domain, and this is coupled to a regular grid-based simulator applied on a narrow band around the liquid interface or solid boundaries. In the context of deep ocean waves, Keeler and Bridson [2014] achieved a surface-only discretization by combining the *El Topo* surface tracker with the solution of a specific boundary integral equation derived under a potential flow assumption. Another use for vorticity equations at the liquid interface is to provide additional detail to a lower resolution fluid simulation [Kim et al. 2009; Bojsen-Hansen and Wojtan 2013], similar in spirit to the use of vortex particles that augment smoke simulations with turbulent detail [Selle et al. 2005; Pfaff et al. 2009].

Vortex Sheets   We make use of a vortex sheet formulation of the vorticity equation. Early numerical work in this direction was carried out by Tryggvason [1988], Agishtein and Migdal [1989], and Pozrikidis [2000] among others. Recently Stock [2006; 2008] proposed a circulation-based discretization that has since been extended to smoke animation [Pfaff et al. 2012; Brochu et al. 2012]. The main source of vorticity for smoke is fluid density gradients (i.e., *baroclinity*), which requires some quantities to be converted back and forth between vorticity and circulation. For bubbles the vorticity source is *surface tension*, which possesses a simple integration rule that works directly in the space of circulations.

3 Smooth Setting

A *soap film* is a thin sheet of liquid immersed in an ambient fluid medium, typically air. When the film has a spherical topology, it is known as a *soap bubble*, and when multiple such bubbles contact, they form a non-manifold network of films known as a *foam*.

We focus on centimeter-scale soap films, whose dynamics are generally dominated by (a) the surface tension of the film, along with (b) the (assumed) incompressibility and (c) inertia of the ambient air. For the centimeter length scale, the inertia of the liquid itself is negligible; the temporal evolution of the film is governed by the motion of the ambient air.

To capture this behavior, we model the interface as a *vortex sheet*.

3.1 Kinematics of a vortex sheet

A vortex sheet is an immersed surface delimiting a discontinuity in (only) the tangential component of a velocity field in 3-space. While the tangential component of velocity is generally discontinuous, the component normal to the vortex sheet remains continuous.

Consider a surface $f : M \to \mathbb{R}^3$ immersed in ambient space, where $M \subset \mathbb{R}^2$ is a reference domain. To each surface point $f(\mathbf{X})$ we associate a unit surface normal $\mathbf{n}(\mathbf{X}) : M \to S^2$.

The state of a vortex sheet is encoded by its position f and a scalar field $\Gamma : M \to \mathbb{R}$ called the *circulation* [Pozrikidis 2000].

Circulation   We note that *circulation* is most typically defined as a quantity associated to a given closed loop; in a slight abuse of terminology, borrowed from other works on vortex sheets [Pozrikidis 2000], we take circulation to be a pointwise quantity, by identifying each point $f(\mathbf{X})$ with an arbitrary loop, as follows.

To understand the geometry behind $\Gamma(\mathbf{X})$, consider an *arbitrary* closed loop L that pierces the sheet at $\mathbf{x} = f(\mathbf{X})$ and some *fixed*

reference point $\mathbf{x}_0 = f(\mathbf{X}_0)$ (refer to the inset figure). $\Gamma(\mathbf{X})$ measures the alignment of the velocity field to tangent motion along the closed loop, i.e.,

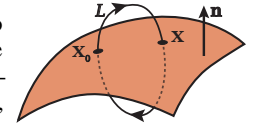$$\Gamma(\mathbf{X}) = \oint_L \mathbf{u} \cdot d\mathbf{x}.$$

Figure 2: *Sign convention for pointwise circulation.*

Above, we emphasized the word *arbitrary* because for any two loops L_1 and L_2 both piercing the sheet only at $\mathbf{x}$ and $\mathbf{x}_0$, $\oint_{L_1} \mathbf{u} \cdot d\mathbf{x} = \oint_{L_2} \mathbf{u} \cdot d\mathbf{x}$ ([Pozrikidis 2000]). We emphasized the word *fixed* because the scalar field Γ is meaningful only if the same reference point $\mathbf{x}_0$ is used for all evaluations of $\Gamma(\mathbf{X}), \mathbf{X} \in M$. Furthermore, selecting a different reference point $\mathbf{x}_0'$ is equivalent to uniformly offsetting the entire field by some fixed constant, $\Gamma'(\mathbf{X}) = \Gamma(\mathbf{X}) + C$. Note that Fig. 2 establishes a correspondence between the orientation of the surface (normal) and the sign of the circulation.

Recovering the ambient velocity from the circulation   With Γ as our state variable, we can evaluate the velocity field in 3-space in two steps. First we recover the *vortex sheet strength*, $\gamma : M \to \mathbb{R}^3$,

$$\gamma = \mathbf{n} \times \nabla_f \Gamma, \tag{1}$$

where ∇_f is the surface gradient operator for f. Observe that by construction γ is tangential to the surface (because of $\mathbf{n}\times$) and divergence-free (because it is a right-angle rotation of a gradient field). Note that the direction of γ is determined by the local $\nabla_f \Gamma$ direction, independent of the choice of the reference point $\mathbf{x}_0$. Vortex sheet strength represents vorticity confined to the sheet, under the relationship $\omega = \gamma \delta(f)$, with Dirac delta δ.
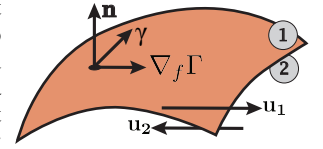

**Figure 3:** *Conventions for vortex sheet strength, for a sheet separating regions 1 and 2.*

From the vortex sheet strength we recover the ambient *velocity*, $\mathbf{u} : \mathbb{R}^3 \to \mathbb{R}^3$ through the Biot-Savart integral

$$\mathbf{u}(\mathbf{x}) = \frac{1}{4\pi} \int_f \frac{\gamma \times (\mathbf{x} - \mathbf{x}')}{\|\mathbf{x} - \mathbf{x}'\|^3} \, df'. \tag{2}$$

The field $\mathbf{u}$ is divergence-free by construction. Thus, a velocity field derived from vortex sheet kinematics is automatically able to capture the dynamics of incompressible fluids without explicit enforcement of the incompressibility condition.

Next, we consider two nearby points $\mathbf{x}$ and $\mathbf{x}'$ on the vortex sheet. The integration loop for circulation at $\mathbf{x}'$ intersects the sheet at $\mathbf{x}'$ and the reference point $\mathbf{x}_0$, and can be broken down as the sum of two loops: one between $\mathbf{x}_0$ and $\mathbf{x}$, and one between $\mathbf{x}$ and $\mathbf{x}'$. The former corresponds to the circulation at $\mathbf{x}$. Therefore, the difference between $\Gamma(\mathbf{X})$ and $\Gamma(\mathbf{X}')$ is the velocity integral around the latter loop, which is represented by the tangential velocity jump $\mathbf{u}$ at $\mathbf{x}$ as the two points approach each other. This reveals the following relation, which is needed in Section 3.3 (see [Pozrikidis 2000] for details):

$$\Delta \mathbf{u} = \nabla_f \Gamma. \tag{3}$$
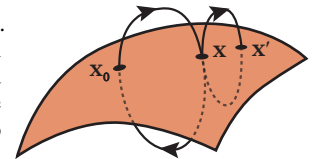
3.2 Dynamics of self-advection

In the absence of external forces, the evolution of the circulation field is given by Kelvin's circulation theorem:

$$\frac{D\Gamma}{Dt} = 0, \tag{4}$$

where D denotes the *total* (equivalently *material* or *advective*) derivative.

Consider the consequences on implementation. As the vortex sheet deforms under the advection induced by the ambient air, the scalar circulation field remains constant. This property sets circulation apart from a vorticity-based representation of the velocity field, avoiding explicit handling of vortex stretching and simplifying the numerical implementation.

3.3 Dynamics with surface tension

With surface tension, the circulation field no longer remains constant; instead its evolution is governed by a simple, local law.

Neglecting viscosity and external forces, we have the momentum equation for the incompressible Euler equations

$$\frac{D\mathbf{u}}{Dt} = -\frac{\nabla p}{\rho} \tag{5}$$

everywhere away from the sheet, where ∇ is the canonical gradient of $\mathbb{R}^3$. Taking the difference of the limiting values across the sheet gives the relation

$$\frac{D\Delta\mathbf{u}}{Dt} = -\frac{\nabla(p_1 - p_2)}{\rho} = -\frac{\nabla_f(p_1 - p_2)}{\rho} \tag{6}$$

on the sheet. For the second equality, we have used the fact that $\nabla(p_1 - p_2) = \nabla_f(p_1 - p_2)$, which holds because the velocity jump $\Delta\mathbf{u}$ is tangential to the surface.

The pressure jump $p_1 - p_2$ is balanced by the surface tension

$$p_1 - p_2 = \sigma(H_1 - H_2), \tag{7}$$

where p_1, p_2 are the pressures on each side of the surface, σ is the surface tension coefficient and H_1, H_2, are the (signed, scalar-valued) mean curvatures of the *two* liquid-air interfaces possessed by a soap film immersed in air. We use the convention that the mean curvature is positive when the interface is convex toward the liquid. For a manifold patch of the vortex sheet we simply have that $H_1 = -H_2$, since the conceptual "two" sides of our idealized thin sheet geometrically coincide while possessing opposing orientations. However, we have explicitly broken out the two contributions as a foreshadowing of our treatment of triple-junctions.

Substituting (3) and (7) into (6) yields

$$\frac{D\nabla_f\Gamma}{Dt} = -\frac{\sigma}{\rho}\nabla_f(H_1 - H_2). \tag{8}$$

By linearity of differentiation, we find $\frac{D\nabla_f\Gamma}{Dt} = \nabla_f\frac{D\Gamma}{Dt}$. Applying this rule and integrating both sides gives

$$\boxed{\frac{D\Gamma}{Dt} = -\frac{\sigma}{\rho}(H_1 - H_2),} \tag{9}$$

where we have chosen to discard the integration constant, recalling that Γ is only defined up to the choice of a constant, equivalently the choice of a reference point. For an alternative derivation, refer to Pozrikidis [2000] who builds on an argument by Baker et al. [1982].

Note that circulation evolves in proportion to the *scalar-valued* mean curvature; this may be contrasted against other representations of the velocity field, for which the consideration of surface tension can involve the *vector-valued* mean curvature normal.

Discussion We have arrived at the temporal evolution of the circulation Γ subject to inertia and surface tension. The attendant evolution of the ambient velocity field thus accounts for **inertia**, **surface tension**, and (due to the Biot-Savart law) **incompressibility**.

The simplicity and locality of the evolution (9) become pronounced when one adopts a Lagrangian discretization of the soap film: the update to the state variables requires simply the evaluation of the mean curvature. To our knowledge this circulation-based temporal evolution of vortex sheets subject to surface tension has not previously been employed to model soap films.

4 Discrete Setting

## 4.1 Spatial discretization

Nonmanifold triangle mesh without boundary We represent the geometry of our discrete soap film using a piecewise linear triangulated surface, i.e., a triangle mesh. The mesh contains non-manifold edges and vertices where soap films meet along *Plateau borders* [Weaire and Hutzler 2001].
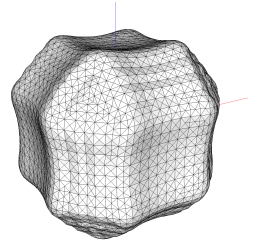
Our mesh is always watertight, i.e., it does not have open boundaries. We accommodate scenarios where the soap film has a prescribed open boundary (e.g., a wire) by ignoring a part of the mesh in the dynamics, as discussed in Section 4.6.

Figure 4: *Oscillating cube.*

Regions We *enumerate* each watertight region of the mesh (i.e., each bubble volume), assigning a unique integer *index* to each region. Two regions with a common interface are called a *region-pair*.

Circulation For the purpose of modeling vortex sheets, we have interpreted circulation as a pointwise quantity [Stock 2006]; that is, it is a scalar field restricted to the surface . Recall that the orientation of the circulation gradient together with the surface normal determines the orientation of the vortex sheet strength: $\gamma = \mathbf{n} \times \nabla_f\Gamma$. We therefore sample the scalar circulation field Γ at *vertices* of the triangle mesh. This gives rise to a piecewise linear field over triangles, whose gradient (and therefore also the sheet-strength) is piecewise constant, and which coincides with the vertex-based discrete curvature measure used below. (This is to be contrasted with previous work which placed pointwise circulation on edges [Stock 2006; Pfaff et al. 2012; Brochu et al. 2012].)
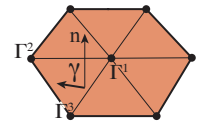
We associate a distinct scalar circulation field to each region-pair. Thus, manifold vertices store one circulation scalar, while triple-junction vertices store *three* circulation scalars, one for each region-pair incident to the vertex. Quadruple-points, which also arise frequently in stable foams, will store *six* circulations, and so forth.

Region-pair interfaces and circulations must satisfy a consistent sign convention. Our implementation chooses the interface normal as

oriented from the higher index region to the lower; the recovered velocity is *independent* of this arbitrary choice, so long as circulation variables are consistently oriented relative to the surface normal, using the convention codified in Fig. 2.

4.2 Temporal discretization

Since we work in the Lagrangian frame of the moving surface, the time-evolution equation for circulation (9) indicates that we can simply advect vertices according to the ambient velocity, and integrate surface tension forces into the vertex-based circulations (§4.3). In the absence of surface tension, circulations are carried along and naturally conserved. We apply forward Euler to integrate the vertex positions under the velocity field $\mathbf{u}$ induced by circulations, as computed from the Biot-Savart law (§4.4).

4.3 Integrating Surface Tension

We integrate surface tension forces into the circulation using the (discrete, scalar, signed, pointwise) mean curvature at the liquid-air interface. Recall that since we have only surface tension forces, and no baroclinic terms, we avoid the need to convert back and forth between circulation and vorticity: integration is performed directly in the space of circulations.

We take a forward Euler step, updating the circulation associated to each region-pair (i, j), $i < j$ via

$$\Delta\Gamma_{i,j}^v = -\frac{\sigma\Delta t}{\rho A}(H_i^v - H_j^v) \qquad (10)$$

where A is the Voronoi area of the vertex [Meyer et al. 2002], used to convert from integrated to pointwise curvature, and H_i^v, H_j^v are the integrated signed scalar mean curvatures at vertex v due to the liquid-air interface at incident regions i and j, respectively. Recall from the smooth setting that H_i^v is positive when region i is outwardly convex at v.

To evaluate H_i^v, we consider only the triangles incident to vertex v and region i. We sum the signed scalar mean curvature of incident edges. For each edge e, we take $H_i^e = |e|\theta$, where $|e|$ is the edge length, and θ_i is the dihedral angle given by $\cos\theta_i = \mathbf{n}_i^1 \cdot \mathbf{n}_i^2$, and $\mathbf{n}_i^1$, $\mathbf{n}_i^2$ are the outwardly oriented normals of the two incident triangles to e for region i [Cohen-Steiner and Morvan 2003]. The sign of H_i^e is unambiguous, based on the outward orientation of region i. Then the signed scalar vertex curvature, H_i^v, is

$$H_i^v = \frac{1}{2}\sum_e H_i^e \qquad (11)$$

where the factor of one half accounts for the fact that the integrated edge curvature is divided amongst its two vertices.

This unified treatment is applied identically whether a vertex lies on simple manifold regions, or on a complex triple, quadruple, or even higher-order junction.
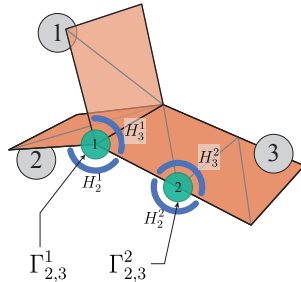
Plateau borders At a triple-junction the total effect of surface tension will be zero on all of the three circulations, $\Gamma_{1,2}^v$, $\Gamma_{1,3}^v$, $\Gamma_{2,3}^v$, only when all three curvatures are equal, $H_1^v = H_2^v = H_3^v$. This recovers the proper $120°$ angle Plateau border equilibrium, as dictated by Plateau's laws, and illustrated in Fig. 5. A similar behavior occurs for quadruple-points, where the four curvatures become equal

with angles of $\theta \approx 109.47°$. Although higher order junctions can also balance in this manner, they are typically unstable.

Figure 5: *A triple-bubble at equilibrium exhibits a stable central Plateau border.*

Discussion For our mean curvature computation, we initially attempted to use the familiar cotan Laplace curvature discretization, which gives rise to a mean curvature normal *vector*, $H\mathbf{n}$; however, our dynamics requires *signed mean curvature scalars*, H. While the latter could theoretically be extracted from the former by an inner product with an appropriately oriented surface normal, we encountered difficulties in the use of various options for discrete vertex normals $\mathbf{n}$. Without a discrete unit normal $\mathbf{n}$ that is guaranteed to be in precise alignment with $H\mathbf{n}$, the scalar mean curvature H extracted from $H\mathbf{n}$ may have an incorrect sign.

4.4 Evaluating Biot-Savart

Given the circulation values stored on each vertex, including multi-valued circulations on non-manifold vertices, we can convert to vortex sheet strength, and use the Biot-Savart law to find the velocity at any point in the domain.

From $\gamma = \mathbf{n} \times \nabla_f \Gamma$ we uniquely recover the vortex sheet strength on a per-triangle basis. The triangle normal $\mathbf{n}$ is computed in standard fashion recalling our earlier orientation convention, and the scalar circulations on the vertices define a linear circulation field on the triangle from which the constant gradient can be readily recovered. Since the vortex sheet strength is a per-triangle quantity, no changes are needed to evaluate Biot-Savart near non-manifold geometry.

Our expression for the Biot-Savart law, with regularization per Pfaff et al. [2012], is:

$$\mathbf{u}(\mathbf{x}) = \frac{1}{4\pi}\int_S \gamma(\mathbf{x}') \times \frac{\mathbf{x} - \mathbf{x}'}{(|\mathbf{x} - \mathbf{x}'| + \alpha^2)^{3/2}}d\mathbf{x}'. \qquad (12)$$

Thus the velocity $\mathbf{u}$ at a point $\mathbf{x}$ in space is an integral over the surface, which we discretize with one-point quadrature at triangle barycenters. We set the regularization parameter α to half the mean mesh edge length. We perform a direct $O(N^2)$ evaluation of this integral; proven FMM [Brochu et al. 2012] or PPPM [Zhang and Bridson 2014] techniques exist to drop this to essentially $O(N)$.

4.5 Integrating Position

The velocity can be evaluated at the mesh vertices in order to perform time integration of the vertex positions. We again use forward Euler, although higher order schemes could be readily incorporated (both here and when integrating surface tension) at the cost of additional Biot-Savart evaluations. Since we use forward Euler to integrate surface tension into circulation (effectively updating velocity), and then use forward Euler to advect positions based on the (updated) velocity, we are in fact applying a Symplectic Euler scheme.

4.6 Solid Interaction

To support simple solid interactions with wire loops (e.g., Fig. 7), we develop a projection method to constrain the motion of the vertices. Given a set of constrained vertices and their desired trajectories, our

approach locally modifies the circulations of the constrained vertices to induce the necessary sheet velocities.

Since the tangential motion of the sheet does not necessarily correspond to tangential motion of the actual liquid film [Pozrikidis 2000], we seek only to constrain the normal motion of the sheet by modifying circulations. In the tangential direction, we simply snap the vertices to their desired position in the tangent plane. This reduces the number of active constraints from $3n$ to n for a set of n constrained vertices. Conveniently, each (manifold) vertex carries a single circulation, giving us exactly n constraints for n degrees of freedom. We can recover a square, dense linear system to find the necessary circulations as follows.

We describe the computation of the Biot-Savart integral for this set of vertices as a matrix B applied to the affected circulation variables, Γ_c, yielding a relation $\mathbf{u} = B\Gamma_c$. We seek a change in circulations $\Delta\Gamma_c$ such that a vertex's normal velocity component changes by $\Delta\mathbf{v} \cdot \mathbf{n}$, where $\Delta\mathbf{v}$ represents the difference between current and target velocity. We must solve the linear system

$$\mathbf{N}^T B \Delta\Gamma_c = \mathbf{N}^T \Delta\mathbf{v} \qquad (13)$$

where N is a matrix composed from the discrete vertex normals of the vertices. For robustness against the possibility of (near-) singularity we employ Tikhonov regularization, by adding the identity matrix scaled such that its influence is small and independent of time step and mesh resolution:

$$(B^T \mathbf{N}\mathbf{N}^T B + \lambda^2 \mathbf{I})\Delta\Gamma_c = B^T \mathbf{N}\mathbf{N}^T \Delta\mathbf{v}, \qquad (14)$$

where $\lambda = 0.025/\bar{e}$ is the regularization parameter, and $\bar{e}$ is the average edge length. This corresponds to a mild preference for smaller changes in circulation. The computed $\Delta\Gamma_c$ is directly added to the circulation variables and the simulation continues.

At times, we would like to animate an *open* soap film bounded by a wire, although the *Los Topos* package currently requires that all regions be closed and watertight. We therefore approximate open scenarios by adding a film of inactive and non-rendered ghost triangles that do not participate in the dynamics (i.e., circulation evolution, Biot-Savart evaluation, etc.), but *do* close up the open region. Moreover, we observe that in the presence of an open boundary, having vorticity in the interior of the soap film is insufficient, since those degrees of freedom cannot adequately encode a path of air flow from below the film to above (and *vice versa*) around the film boundary. As a result the flow behaves as if the air volumes above and below the film are conserved separately, even though the two regions are well connected outside the sheet boundary. The top row of Figure 6 illustrates this phenomenon in 2D. We therefore place an additional vorticity degree of freedom on each open boundary edge along the edge tangent direction (Figure 6 bottom row), and solve for their strength using the same projection method above.

5 Time Integration

Our complete time integration loop is given by Algorithm 1.

Algorithm 1 Time Integration Loop

---

while simulating **do**
    Integrate Surface Tension into Circulations (§4.3)
    Recover Velocity from Circulation (Biot-Savart) (§4.4)
    Integrate Vertex Positions Using Velocity (§4.5)
    Enforce Constraints via Projection (§4.6)
    Perform Remeshing and Topology Changes, *Los Topos* (§5.1)
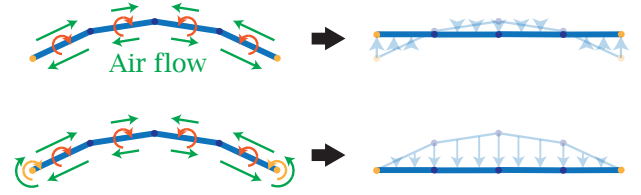**end while**

Figure 6: *2D illustration of the treatment of vorticity at open boundary. The thick blue lines are the vortex sheet, with the yellow dots being the boundary. Top: The interior vorticity (orange arrows) lacks the ability to represent an airflow path from below to above the sheet. Bottom: The additional vorticity degrees of freedom (yellow) provides the airflow path around the open boundary.*
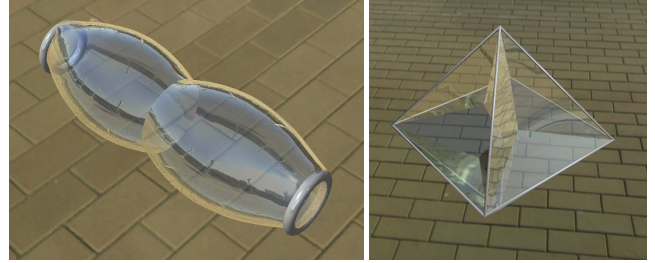

Figure 7: *Left:A double-bubble being gradually pulled apart by two wire loop (constraints) on either end. Right:A stable non-manifold film structure spanning an octahedron-shaped wire.*

5.1 Discrete Mesh Evolution

Our discrete soap film model relies on the ability to represent non-manifold liquid interfaces as Lagrangian triangle meshes, and to treat the topological changes that arise as bubbles deform and rearrange. We make use of the *Los Topos* multimaterial surface tracking package introduced by Da et al. [2014], which was tailor-made for these types of topology changes, including bubble splitting, multi-bubble merging, and so-called T1 processes (essentially foam rearrangement).

We treat *Los Topos* largely as a black box: we provide proposed vertex trajectories for the vertices of the triangle mesh, and the algorithm finds an updated watertight mesh that satisfies these trajectories as nearly as possible, after handling topological changes and remeshing. Since we rely on storing circulation data at mesh vertices, we must also reassign circulation values to affected vertices whenever a remeshing operation is performed. We therefore use a slightly smaller set of operations to reduce resampling: edge splitting, edge collapse, T1 processes, and snapping. For edge splitting, edge collapse, or snapping (coalescing nearby unconnected vertices), we project the new vertex position onto the old mesh and compute a new circulation value by barycentric interpolation over triangles. For a T1 process, which amounts to duplicating and separating an existing vertex, the two resulting vertices are assigned the circulation of the old vertex. (We eschew edge flipping, which changes geometry without changing vertices leading to temporal discontinuities, and vertex smoothing, which moves nearly all vertices and leads to oversmoothing of circulation.)

6 Results

We illustrate the effectiveness of our method with a range of examples. The results are organized to show how our method effectively preserves circulation, handles solid boundaries, and stably simu-

Test	Vertices	Faces	Simulation time per frame (s)	Number of frames	Total time (min)
Cube oscillation	4274	8544	1.29	6736	145
Double bubble	5204	10496	1.94	3560	115
Octahedron	854	1951	0.319	564	3
Bubble in a ring	1122	2240	0.309	1533	8
Catenoid pinching	1153	2294	0.96	1500	24
Pulling double bubble apart	1003	1998	0.276	5000	23
Bubble cluster	2734	5787	0.695	2214	25
Bubble popping	1971	4099	0.321	28000	150
Sweeping ring	3070	6129	0.504	7500	63

Table 1: *Simulation time for various examples. A frame always corresponds to one time step of simulation.*

lates non-manifold foam configurations. The size of the simulation meshes and simulation times are summarized in Table 1. The maximum percentage deviations in the total volume of enclosed air over the entire simulations for the cube, double-bubble, and foam rearrangement examples was 2.2%, 2.4%, and 0.05% respectively.

Circulation preservation The circulation-based discretization in Section 4 allows our bubbles to preserve circulation over long simulations while being relatively insensitive to the effects of remeshing. Figure 4 uses an initially cube-shaped bubble to illustrate how our method maintains bubble oscillations over very long periods. The bubble remains stable and temporally smooth despite re-meshing and re-sampling the circulation variables as often as needed to preserve mesh quality. The sphere also maintains a remarkable degree of symmetry throughout.
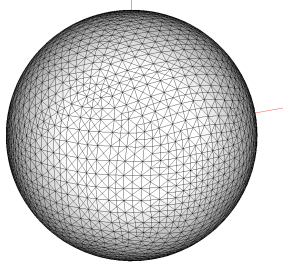

Figure 8: *The equilibrium bubble.*

Note that our explicit integration scheme is not unconditionally stable, and we must introduce some damping (by slightly diffusing Γ along the sheet) in order to maintain stability. Conveniently however, this can also provide a reasonable visual approximation of air viscosity, as we demonstrate by re-running the same oscillating cube bubble with a substantially increased damping coefficient. As expected it settles rapidly to a stable spherical configuration (Fig. 8), demonstrating that our method achieves the desired steady-state equilibrium for this canonical example.

Moving beyond the simple sphere topology, we perform a similar oscillation test on an initially stretched *double bubble*, shown inset. Here, and throughout our examples, the velocity of the ambient air flow plays the dominant role in the motion, in this case generating the interesting wobbling behavior; this velocity is compactly encoded by the triangle mesh.

Figure 9: *A double-bubble.*

Furthermore, we see that surface tension behaves naturally on the triple curves and the interior interface joining the two bubbles.

Interaction with solid boundaries Our solid boundary condition explained in Section 4.6 allows us to simply and stably simulate bubbles interacting with solid obstacles like metal wires or bubble wands. Figure 1, center, shows how pulling apart two metal rings

can correctly stimulate the catenoid soap film shape and eventual separation of a single soap film. Here we have also made use of non-simulated triangles to illustrate that our numerical method supports open films (although our underlying surface tracker does not). When the separation occurs, sharp geometric features are created near-instantaneously, but again the simulation remains stable.

Figure 7, left, shows a double-bubble being pulled apart by two metal rings until they undergo splitting and become fully separated. While the pinching behavior is similar to the catenoid case, here we see a triple junction curve shared by two bubbles collapsing to a point and separating as opposed to the earlier example involving the collapse of a single film.

Figure 1, right, illustrates a squished bubble constrained by a stationary loop. The surface tension forces lead the bubble to gradually squeeze to one side as the combined system relaxes towards a more stable configuration. Such an example would be difficult to achieve with a standard Eulerian scheme due to the complex boundary conditions created by the wire.
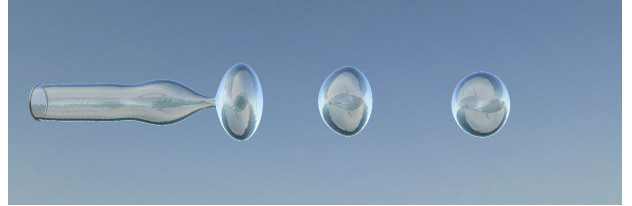

Figure 10: *Sweeping a metal ring through space to blow bubbles.*

Figure 10 simulates blowing bubbles from a wire ring, by sweeping the ring through space in the axial direction. The inertia of the air mass pushes the initially flat soap film to bulge out until it pinches off into individual bubbles.

Non-manifold foam dynamics Next we step from single and double film and bubble configurations up to the more general case of highly complex non-manifold film and foam structures. Figure 7, right, shows a network of non-manifold soap films stretched over an octahedron, a common physics experiment for children. We initialize the geometry a short distance from its equilibrium, and observe that it quickly settles and remains stable.

Our final pair of test cases involves a free-floating foam consisting of ten bubbles combined together in a complicated, non-manifold non-equilibrium state (Fig. 1, left). Upon initiating the dynamics, the bubbles naturally shift and rearrange until they find an equilibrium. To up the ante, we take the same drifting foam and intermittently puncture a random bubble by directly deleting the relevant interface triangles. At each pop the foam suddenly ripples and the bubbles quickly shift into new non-manifold equilibrium configurations in accordance with the dynamical laws.

7 Discussion

We have approached foam simulation from a markedly different direction than earlier alternatives, yielding a number of trade-offs, including limitations.

From the standpoint of versatility, purely Eulerian methods currently dominate. Given their long line of investigation, Eulerian methods support a broad range of features that we have yet to explore, including accurate modeling of viscosity, application to volumetric liquids, and bidirectional coupling with complex rigid and deformable objects. On the other hand, Eulerian methods require that bubbles be significantly larger than the grid scale in order to resolve the desired velocity field and film geometry without excessive dissipation or volume loss; even then, explicit volume control may be necessary. Although circulation- or energy-preservation has been considered by a few Eulerian schemes [Elcott et al. 2007; Mullen et al. 2009], conserving these quantities in an Eulerian setting remains challenging in the presence of fluid interfaces. In contrast to Eulerian methods, our approach efficiently handles all the dynamics on the mesh surface itself, notably without the need for a large linear solve; furthermore, circulation is preserved in a natural and simple manner, and in particular in the presence of non-manifold fluid interfaces.

In comparison to related surface-based discretizations of thin sheets and films [Batty et al. 2012; Zhu et al. 2014], our focus on centimeter-scale soap films justifies neglecting certain quantities: we do not track mass or thickness of the liquid, nor *tangential* component of the dynamics. Instead, we focus on the complex geometry of non-manifold foam structures and its attendant topology changes, moreso than any existing purely triangle mesh-based scheme for foam. Our treatment of air-dominated dynamics also requires no coupling with a grid-based solver.

Some of our method's limitations appear to be inherent to the vortex sheet model, but many offer exciting directions for future investigation. Our current derivation assumes inviscid incompressible flow, so that proper viscous boundary layers (e.g., vortex shedding) and divergent flows (e.g., inflating bubbles) remain out of reach; it may be interesting to introduce a limited form of divergence in the form of normal motion, via an operator splitting approach. The assumption of equal densities on either side of the sheet removes the baroclinic terms, which play a crucial role in previous vortex sheet smoke methods as well as potential extensions to small-scale liquid droplets. There is also ample room for further acceleration [Brochu et al. 2012; Zhang and Bridson 2014], as the method currently relies on a direct Biot-Savart evaluation that scales quadratically and explicit time integration of notoriously stiff surface tension forces.

We believe our circulation-based discretization is attractive both for its minimalist representation of complex soap film dynamics, and for the concrete numerical and computational benefits it offers. We have shown that it preserves volume effectively and exhibits minimal dissipation, while being fast and stable enough to handle a range of compelling foam and bubble behaviors. Having so far addressed the dynamics of both turbulent smoke and soap foams, we anticipate that vortex sheet techniques have a great deal yet to offer.

Acknowledgments

References

AGISHTEIN, M. E., AND MIGDAL, A. A. 1989. Dynamics of vortex surfaces in three dimensions: Theory and simulations. *Physica D: Nonlinear Phenomena 40*, 1, 91–118.

ANGELIDIS, A., AND NEYRET, F. 2005. Simulation of smoke based on vortex filament primitives. In *Symposium on Computer Animation*, 87 – 96.

ANGELIDIS, A., NEYRET, F., SINGH, K., AND NOWROUZEZAHRAI, D. 2006. A controllable, fast and stable basis for vortex based smoke simulation. In *Symposium on Computer Animation*, 25–32.

BAKER, G. R., MIRRON, D. I., AND ORSZAG, S. A. 1982. Generalized vortex methods for free-surface flow problems. *J. Fluid Mech. 123*, 477–501.

BARNAT, A., AND POLLARD, N. S. 2012. Smoke sheets for graph-structured vortex filaments. In *Symposium on Computer Animation*, 77–86.

BATTY, C., URIBE, A., AUDOLY, B., AND GRINSPUN, E. 2012. Discrete viscous sheets. *ACM Trans. Graph. (SIGGRAPH) 31*, 4, 113.

BOJSEN-HANSEN, M., AND WOJTAN, C. 2013. Liquid surface tracking with error compensation. *ACM Trans. Graph. (SIGGRAPH) 32*, 4, 79:1–79:10.

BRAKKE, K. 1992. The surface evolver. *Experimental Mathematics 1*, 2, 141–165.

BROCHU, T., AND BRIDSON, R. 2009. Robust topological operations for dynamic explicit surfaces. *SIAM J. Sci. Comput. 31*, 4, 2472–2493.

BROCHU, T., KEELER, T., AND BRIDSON, R. 2012. Linear-time smoke animation with vortex sheets. In *Symposium on Computer Animation*, 87–95.

BROCHU, T. 2006. *Fluid animation with explicit surface meshes and boundary-only dynamics*. Master's thesis, Citeseer.

BUSARYEV, O., DEY, T. K., WANG, H., AND REN, Z. 2012. Animating bubble interactions in a liquid foam. *ACM Trans. Graph. (SIGGRAPH) 31*, 4, 63.

CLAUSEN, P., WICKE, M., SHEWCHUK, J. R., AND O'BRIEN, J. F. 2013. Simulating liquids and solid-liquid interactions with Lagrangian meshes. *ACM Trans. Graph. 32*, 2, 17.

COHEN-STEINER, D., AND MORVAN, J.-M. 2003. Restricted delaunay triangulations and normal cycle. 237–246.

COTTET, G.-H., AND KOUMOUTSAKOS, P. 2000. *Vortex Methods: Theory and Practice*. Cambridge University Press.

DA, F., BATTY, C., AND GRINSPUN, E. 2014. Multimaterial mesh-based surface tracking. *ACM Trans. Graph. (SIGGRAPH) 33*, 4, 112:1–112:11.

DURIKOVIC, R. 2001. Animation of soap bubble dynamics, cluster formation and collision. *Computer Graphics Forum (Eurographics) 20*, 3, 67–76.

ELCOTT, S., TONG, Y., KANSO, E., SCHRÖDER, P., AND DESBRUN, M. 2007. Stable, circulation-preserving, simplicial fluids. *ACM Trans. Graph. 26*, 1, 4.

GLASSNER, A. 2000. Soap bubbles: Part 1. *IEEE Computer Graphics and Applications 20*, 5, 76–84.

GLASSNER, A. 2000. Soap bubbles: Part 2. *IEEE Computer Graphics and Applications 20*, 6, 99–109.

GOLAS, A., NARAIN, R., SEWALL, J., KRAJCEVSKI, P., DUBEY, P., AND LIN, M. C. 2012. Large-scale fluid simulation using velocity-vorticity domain decomposition. *ACM Trans. Graph. (SIGGRAPH Asia) 31*, 6, 148.

GREENWOOD, S. T., AND HOUSE, D. H. 2004. Better with bubbles. In *Symposium on Computer Animation*.

HONG, J.-M., AND KIM, C.-H. 2003. Animation of bubbles in liquid. *Computer Graphics Forum 22*, 3, 253–262.

HONG, J.-M., AND KIM, C.-H. 2005. Discontinuous fluids. *ACM Trans. Graph. (SIGGRAPH) 24*, 3 (July), 915–920.

HONG, J.-M., LEE, H.-Y., YOON, J.-C., AND KIM, C.-H. 2008. Bubbles Alive. *ACM Trans. Graph. (SIGGRAPH) 27*, 3, 48.

KANG, M., FEDKIW, R., AND LIU, X.-D. 2000. A boundary condition capturing method for multiphase incompressible flow. *SIAM J. Sci. Comput. 15*, 3, 323–360.

KEELER, T., AND BRIDSON, R. 2014. Ocean waves animation using boundary integral equations and explicit mesh tracking. In *Symposium on Computer Animation*.

KIM, B., LIU, Y., LLAMAS, I., JIAO, X., AND ROSSIGNAC, J. 2007. Simulation of bubbles in foam with the volume control method. *ACM Trans. Graph. (SIGGRAPH) 26*, 3, 98.

KIM, D., SONG, O.-Y., AND KO, H.-S. 2009. Stretching and wiggling liquids. *ACM Trans. Graph. (SIGGRAPH Asia) 28*, 5, 120.

KIM, D., SONG, O.-Y., AND KO, H.-S. 2010. A practical simulation of dispersed bubble flow. *ACM Trans. Graph. (SIGGRAPH) 29*, 4, 70.

KUCK, H., VOGELSANG, C., AND GREINER, G. 2002. Simulation and rendering of liquid foams. In *Graphics Interface*, 81–88.

LOSASSO, F., SHINAR, T., SELLE, A., AND FEDKIW, R. 2006. Multiple interacting liquids. *ACM Trans. Graph. (SIGGRAPH) 25*, 3, 812–819.

MEYER, M., DESBRUN, M., SCHRÖDER, P., AND BARR, A. 2002. Discrete differential-geometry operators for triangulated 2-manifolds. In *VisMath*, Springer-Verlag, Berlin, Germany, 35–54.

MIHALEF, V., UNLUSU, B., METAXAS, D., SUSSMAN, M., AND HUSSAINI, M. Y. 2006. Physics based boiling simulation. In *Symposium on Computer Animation*, 317–324.

MISZTAL, M., ERLEBEN, K., BARGTEIL, A. W., CHRISTENSEN, B. B., BAERENTZEN, A., AND BRIDSON, R. 2012. Multiphase flow of immiscible fluids on unstructured moving meshes. In *Symposium on Computer Animation*, Eurographics Association, Lausanne, Switzerland, 97–106.

MULLEN, P., CRANE, K., PAVLOV, D., TONG, Y., AND DESBRUN, M. 2009. Energy-preserving integrators for fluid animation. *ACM Trans. Graph. (SIGGRAPH) 28*, 3, 38.

PAN, H., CHOI, Y.-K., LIU, Y., HU, W., DU, Q., POLTHIER, K., ZHANG, C., AND WANG, W. 2012. Robust modeling of constant mean curvature surfaces. *ACM Trans. Graph. (SIGGRAPH) 31*, 4, 85.

PARK, S. I., AND KIM, M. J. 2005. Vortex fluid for gaseous phenomena. In *Symposium on Computer Animation*, 261–270.

PATKAR, S., AANJANEYA, M., KARPMAN, D., AND FEDKIW, R. 2013. A Hybrid Lagrangian-Eulerian Formulation for Bubble Generation and Dynamics. In *Symposium on Computer Animation*, 105–114.

PFAFF, T., THUEREY, N., SELLE, A., AND GROSS, M. 2009. Synthetic turbulence using artificial boundary layers. *ACM Trans. Graph. (SIGGRAPH Asia) 28*, 5, 121.

PFAFF, T., THUEREY, N., AND GROSS, M. 2012. Lagrangian vortex sheets for animating fluids. *ACM Trans. Graph. (SIGGRAPH) 31*, 4, 112:1–112:8.

PINKALL, U., AND POLTHIER, K. 1993. Computing discrete minimal surfaces and their conjugates. *Experimental Mathematics 2*, 1, 15–36.

POZRIKIDIS, C. 2000. Theoretical and computational aspects of the self-induced motion of three-dimensional vortex sheets. *J. Fluid Mech. 425*, 335–366.

SAYE, R., AND SETHIAN, J. 2013. Multiscale Modeling of Membrane Rearrangement, Drainage, and Rupture in Evolving Foams. *Science 340*, 6133, 720–724.

SELLE, A., RASMUSSEN, N., AND FEDKIW, R. 2005. A vortex particle method for smoke, water and explosions. *ACM Trans. Graph. (SIGGRAPH) 24*, 3, 910–914.

STOCK, M. J., DAHM, W. J. A., AND TRYGGVASON, G. 2008. Impact of a vortex ring on a density interface using a regularized inviscid vortex sheetmethod. *J. Comp. Phys. 227*, 21, 9021–9043.

STOCK, M. 2006. *A regularized inviscid vortex sheet method for three-dimensional flows with density interfaces*. PhD thesis.

TRYGGVASON, G. 1988. Numerical simulations of the Rayleigh-Taylor instability. *J. Comp. Phys. 75*, 2, 253–282.

VINES, M., HOUSTON, B., LANG, J., AND LEE, W.-S. 2014. Vortical inviscid flows with two-way solid-fluid coupling. *IEEE TVCG 20*, 2, 303–315.

WEAIRE, D., AND HUTZLER, S. 2001. *Physics of Foams*. Oxford University Press, New York.

WEAIRE, D. 2013. A fresh start for foam physics. *Science 340*, 6133, 693–694.

WEISSMANN, S., AND PINKALL, U. 2009. Real-time interactive simulation of smoke using discrete integrable vortex filament. In *VRIPHYS*, 1–10.

WEISSMANN, S., AND PINKALL, U. 2010. Filament-based smoke with vortex shedding and variational reconnection. *ACM Trans. Graph. (SIGGRAPH) 29*, 4, 115:1–115:12.

ZHANG, X., AND BRIDSON, R. 2014. A PPPM fast summation method for fluids and beyond. *ACM Trans. Graph. (SIGGRAPH Asia) 33*, 6, 206.

ZHANG, Y., WANG, H., WANG, S., TONG, Y., AND ZHOU, K. 2012. A deformable surface model for real-time water drop animation. *IEEE TVCG 18*, 8, 1281–1289.

ZHENG, W., YONG, J.-H., AND PAUL, J.-C. 2006. Simulation of bubbles. In *Symposium on Computer Animation*, Eurographics Association, Vienna, 325–333.

ZHU, B., QUIGLEY, E., CONG, M., SOLOMON, J., AND FEDKIW, R. 2014. Codimensional surface tension flow on simplicial complexes. *ACM Trans. Graph. (SIGGRAPH) 33*, 4, 111.